AIAA JOURNAL
Vol. 45, No. 8, August 2007

Real-Gas Extensions to Tangent-Wedge and Tangent-Cone Analysis Methods

Stephen A. Whitmore*
Utah State University, Logan, Utah 84322-4130

DOI: 10.2514/1.28521

Engineering codes are powerful tools for the conceptual design stage. Use of these codes in early design stages enables higher fidelity computational fluid dynamics calculations or wind-tunnel tests to be performed on more mature configurations. Two widely used engineering tools for conceptual level supersonic/hypersonic aerodynamic prediction are tangent-wedge and tangent-cone methods. Unfortunately, these analysis tools lack the ability to systematically account for effects of real-gas flow across the oblique shock wave. This paper derives an extension to the classical oblique shock wave equations where the effects of real-gas flow changes are modeled using theoretical models borrowed from statistical mechanics. Using an enthalpy balance across the shock wave, the Einstein model for a diatomic gas is analytically integrated to give a relationship of temperature, ratio of specific heats, and velocity on the downstream side of the shock wave. This relationship replaces the energy equation used in the ideal-gas oblique shock analysis. This method is adapted to conical flowfield assuming an initial shock angle, and using the new oblique shock algorithm to compute properties immediately behind the conical shock. The resulting model is compared to equilibrium real-gas calculations and shown to give accurate results well into the hypersonic flow regime, approximately Mach 20.

Nomenclature

C_p	=	specific heat at constant pressure, J/kg · K
C_{p1}	=	specific heat at constant pressure upstream of shock wave, J/kg · K
C_v	=	specific heat at constant volume, J/kg · K
const	=	generic constant
e	=	gas internal energy per unit mass, J/kg
$e_{\text{electronic}}$	=	energy per unit mass of molecule electron clouds, J/kg
$f()$	=	Newton–Raphson solver symbolic function, K
$g()$	=	Newton–Raphson solver symbolic function, K
$\mathcal{H}$	=	Plank's constant, $6.626 - 693 \times 10^{-34}$ J · s
h	=	gas enthalpy per unit mass, J/kg
h_0	=	stagnation enthalpy per unit mass, J/kg
j	=	outer loop iteration index
M_w	=	molecular weight, kg/kg · mol
M_1	=	Mach number upstream of shock wave or freestream temperature
M_2	=	Mach number downstream of shock wave
n	=	inner loop iteration index
P	=	generic pressure term, kPa
p_{cone}	=	pressure on surface of cone term, kPa
p_1	=	pressure upstream of oblique shock wave, kPa
p_2	=	pressure downstream of oblique shock wave, kPa
R_g	=	gas-specific constant, R_u/M_W, J/kg · K
R_u	=	universal-gas constant, 8314.4126, J/kg · K
T	=	generic temperature term, K
T_{cone}	=	inviscid flow temperature on surface of cone term, K
T_r	=	quantum temperature, K
T_1	=	temperature upstream of shock wave or freestream temperature, K
T_2	=	temperature downstream of shock wave, K
T_0	=	generic stagnation temperature term, K
T_{01}	=	stagnation temperature upstream of shock wave, K
T_{02}	=	stagnation temperature downstream of shock wave, K
u_1	=	upstream velocity component normal to oblique shock wave, m/s
u_2	=	downstream velocity component normal to oblique shock wave, m/s
V	=	generic velocity term, m/s
$V_{\max}$	=	maximum velocity in a conical flowfield, m/s
V_1	=	velocity upstream of shock wave or freestream velocity, m/s
V_2	=	velocity downstream of shock wave, m/s
w_1	=	upstream velocity component tangent to oblique shock wave, m/s
w_2	=	downstream velocity component tangent to oblique shock wave, m/s
β	=	shock wave angle relative to freestream flow, deg
β_{shock}	=	assumed conical shock wave angle, deg
γ	=	ratio of specific heats at constant pressure and constant volume
γ_1	=	ratio of specific heats upstream of shock wave
γ_2	=	ratio of specific heats downstream of shock wave
δ	=	outer loop convergence criterion
δ_{shock}	=	flow direction angle immediately behind conical shock wave, deg
ε	=	inner loop convergence criterion
θ	=	flow turning or wedge angle, deg
θ_{cone}	=	half-angle of cone surface, deg
κ	=	Boltzmann constant, $1.3806503 \times 10^{-23}$ J/K
ν	=	principal vibrational mode of the molecule, Hz
ρ_1	=	density upstream of oblique shock wave, kg/m^3
ρ_2	=	density downstream of oblique shock wave, kg/m^3
ϑ	=	normalized velocity parameter for conical flow, $V/V_{\max}$
ϑ_r	=	normalized conical flow velocity parallel to radial direction
ϑ_θ	=	normalized conical flow velocity perpendicular to radial direction
∂	=	partial differential operator

Received 24 October 2006; revision received 1 February 2007; accepted for publication 12 February 2007.

*Assistant Professor, Mechanical and Aerospace Engineering Department, 4130 Old Main Hill/UMC 4130. Associate Fellow AIAA.

I. Introduction

ADVANCES in computer execution speed, memory capacity, and user interactivity have allowed the application of numerical techniques in computational fluid dynamics (CFD) to grow rapidly in the last decade. However the cost, sheer volume of labor, and required setup and computational time still preclude the use of CFD during the early design stages of flight vehicles. For conceptual design "engineering codes" are still the preferred method for vehicle designers. Engineering codes are powerful tools when applied in the conceptual design stage. Their use in the early stages of design enables higher fidelity CFD calculations or wind-tunnel tests to be performed on more mature vehicle concepts and can trim many months off of the design process. Most of classical engineering design techniques have been proven over the years as reliable and give highly representative aerodynamic predictions.

The use of engineering tools early in the design process is especially important for high-speed supersonic or hypersonic vehicle designs. At high speeds aerothermodynamic interactions become complex, gas properties change rapidly, and CFD solutions require very large amounts of setup and execution time, and still often do not produce accurate results. Two widely used engineering codes for conceptual level supersonic/hypersonic aerodynamic prediction are Missile DATCOM [1] and S/HABP [2]. Missile DATCOM is a semi-empirical code that calculates the forces and moments on a cylindrical or nearly cylindrical body, with small protuberances and axisymmetric fin sets. This code can be applied over a wide range of Mach numbers. Some known errors will occur in using Missile DATCOM to analyze hypersonic designs and the preferred hypersonic code is S/HABP (supersonic/hypersonic arbitrary body program). S/HABP uses first-order methods [3] such as modified Newtonian flow, tangent wedge, or tangent cone to calculate the pressures on arbitrarily shaped bodies and lifting surfaces at supersonic and hypersonic speeds.

The tangent-wedge and tangent-cone methods are approximations where the surface properties of a body with a relatively sharp leading edge are constructed by assuming a wedge tangent to a given point on the body and allowing that the properties at that point on the wedge are the same as those at the same point on the original body. Instead of calculating the flowfield around the body itself, simple oblique shock theory can be applied to the constructed wedge shape to determine the desired surface pressure, local Mach number, and inviscid flow temperature. The tangent-cone method is a similar idea in which the actual body is approximated as a cone-shaped axisymmetric body and the local flow properties are assumed to be identical to a conical body with the same local incidence angle. The tangent-wedge method is most accurate for two-dimensional shapes like flaps, wings, and control surfaces. The tangent-cone method is most accurate for slender axisymmetric or three-dimensional shapes like missile forebodies or fuselages. The wedge and cone methods are commonly used in hypersonic analysis methods because they are relatively simple but yield surprisingly accurate results. The conical flow technique is particularly popular and is frequently used to construct hypersonic flowfields from which wave riders are designed [4]. Recently published work [5] has established a theoretical basis for understanding why these techniques yield such accurate results.

Unfortunately, the tangent-wedge and tangent-cone analysis tools have always missed a key element necessary for accurate hypersonic flowfield design, and that is the ability to systematically account for the effects of real-gas flow across the oblique shock wave. These effects have typically been accounted for using ad hoc methods such as Eckert's [6] empirical reference temperature and table lookups of real-gas enthalpy tables to "smear" the gas properties across the shock wave. Clearly, improvements in the management of real-gas effects in the tangent-wedge and tangent-cone engineering analysis tools would be greatly welcomed. This paper derives an extension to the classical oblique shock wave equations where the effects of real-gas changes across the shock wave are modeled using theoretical models borrowed from statistical mechanics. The oblique shock wave model extensions are directly applicable for use in tangent-wedge engineering models. The methods are modified for conical (tangent-cone) flowfields by assuming an initial shock angle, and using the modified oblique shock algorithm to compute the properties immediately behind the conical shock wave. These properties become the initial conditions from which the conical flowfield is solved.

For many applications where a simple, surface inclination method is to be used for a "fast," initial estimate of the integrated inviscid forces (lift and drag) on a hypersonic body, the inclusion of "real-gas effects" may not be warranted due to the additional computational complexity of the real-gas adjustment. However, for designs that must consider the implications of real-gas effects on the thermal design of the vehicle, it is believed that this addition is highly warranted in that it will allow for a less conservative thermal analysis and can save considerably in the overall vehicle weight.

It must be cautioned that the model derived in this paper is strictly valid only for diatomic gases (like air) where there is only one vibration mode present. For triatomic and multi-atomic gases like C02 and CH4, there are additional degrees of freedom that must be accounted for. The methods described herein can be used for this extension; however, the details of that process are beyond the intended scope of this paper. Similar cautions must be expressed with regard to rarefied flowfields. At high hypersonic speeds for entry vehicles, the altitude may be high enough such that the atmosphere is rarefied. Behind the nose shock, however, the flow has continuum properties. Such effects are nearly impossible to account for using first-order engineering tools. This idea must be kept in mind when the algorithm is applied and compared to any flight or test data.

Finally, at very high ambient temperatures such as in combustion flows, or for very high (orbital velocities), gas dissociation may occur and the model predictions become increasingly inaccurate as the degree of dissociation becomes more and more significant. The effects of dissociation are described at length later in this paper.

II. Algorithm Derivation

For a hypersonic flight regime where gas dissociation occurs, in general the flow enthalpy is a function of temperature and pressure and the specific heats of the gas can be related to the change in enthalpy and internal energy by

$$\frac{\partial h}{\partial T} = c_p(T, P) \tag{1a}$$

$$\frac{\partial e}{\partial T} = c_v(T, P) \tag{1b}$$

For flight conditions where gas dissociation does not occur, that is for a single species gas concentration, the specific heats are strongly a function of temperature and weakly a function of pressure. This physical situation frequently occurs behind hypersonic oblique, conical, or detached shock waves away from the stagnation point. Here the shock wave is angled relative to the incoming flow and the subsequent compression and temperature rise is sufficient to excite vibrational modes of the gas molecules, but insufficient to cause gas dissociation.

A. Einstein Statistical Thermodynamics Model

For engineering purposes, the Einstein [7,8] model for a diatomic gas can be used to approximate the changes in internal energy as a function of local flow temperature. For a diatomic gas the internal energy is

$$e(T) = \frac{3}{2}R_gT + R_gT + \frac{h\nu/\kappa T}{\{e^{\frac{h\nu}{\kappa T}} - 1\}}R_gT + e_{\text{electronic}} \tag{2}$$

In Eq. (2) the first two terms on the right-hand side of the equation represent the translational and rotational energies of the gas molecules, the third term represents the vibrational energies of the molecules, and the final term represents the energies of the electron clouds. The electronic energy is independent of the gas temperature. In the vibrational energy term h is Plank's constant, ν is the principal

vibration mode of the molecule, κ is Boltzmann's constant, and R_g is the gas constant for the gaseous mixture. Collectively, the quantity $h\nu/k$ is referred to as the quantum or Einstein temperature T_r. For air the quantum temperature is approximately 3070 K [9]. The specific heat at constant volume is calculated from Eq. (2) by letting

$$c_v = \frac{\partial e}{\partial T} = \left[\frac{5}{2} + \frac{e^{\frac{T_r}{T}}(T_r/T)^2}{\{e^{\frac{T_r}{T}} - 1\}^2}\right] R_g \tag{3}$$

The specific heat at constant pressure is

$$c_p = R_g + c_v = R_g\left[1 + \frac{5}{2} + \left(\frac{T_r}{T}\right)^2 \frac{e^{\frac{T_r}{T}}}{\{e^{\frac{T_r}{T}} - 1\}^2}\right]$$
$$= R_g\left[\frac{7}{2} + \left(\frac{T_r}{T}\right)^2 \frac{e^{\frac{T_r}{T}}}{\{e^{\frac{T_r}{T}} - 1\}^2}\right] \tag{4}$$

Equation (4) will be used to model the change in specific heat across the oblique hypersonic shock wave.

B. Enthalpy Balance Across Nonideal Shock Wave for Constant Species Gas

Conservation of energy requires that the flow enthalpy be conserved across the shock wave, thus

$$h_0 = h + \frac{V^2}{2} = \text{const} \tag{5}$$

Taking the differential of Eq. (5)

$$\partial h + \partial\left[\frac{V^2}{2}\right] = 0 = \partial h + V\partial V \tag{6}$$

Substituting in Eq. (1a) for ∂h and integrating across the shock wave from state 1 to state 2

$$\int_{T_1}^{T_2} c_p(T)\partial T + \int_{V_1}^{V_2} V\partial V = \int_{T_1}^{T_2} c_p(T)\partial T + \frac{V_2^2 - V_1^2}{2} = 0 \tag{7}$$

Letting

$$\int_{T_1}^{T_2} c_p(T)\partial T = \int_{T_1}^{T_2} R_g\left[\frac{7}{2} + \left(\frac{T_r}{T}\right)^2 \frac{e^{\frac{T_r}{T}}}{\{e^{\frac{T_r}{T}} - 1\}^2}\right] \mathrm{d}T \tag{8}$$

and integrating the "easy part" of Eq. (8) first

$$\int_{T_1}^{T_2} c_p(T)\partial T = \left(\frac{7}{2}R_g T_2 - \frac{7}{2}R_g T_1\right)$$
$$+ R_g \int_{T_1}^{T_2}\left[\left(\frac{T_r}{T}\right)^2 \frac{e^{\frac{T_r}{T}}}{\{e^{\frac{T_r}{T_o}} - 1\}^2}\right] \mathrm{d}T \tag{9}$$

Now integrating the "hard part" gives

$$\int_{T_1}^{T_2} c_p(T)\partial T = \left(\frac{7}{2}R_g T_2 + \frac{R_g T_r}{\{e^{\frac{T_r}{T_2}} - 1\}}\right) - \left(\frac{7}{2}R_g T_1 + \frac{R_g T_r}{\{e^{\frac{T_r}{T_1}} - 1\}}\right) \tag{10}$$

Substituting Eq. (10) into Eq. (7) and collecting terms

$$T_2 + \frac{V_2^2}{2(\frac{7}{2}R_g)} + \frac{2}{7}\frac{T_r}{\{e^{\frac{T_r}{T_2}} - 1\}} = T_1 + \frac{V_1^2}{2(\frac{7}{2}R_g)} + \frac{2}{7}\frac{T_r}{\{e^{\frac{T_r}{T_1}} - 1\}} \tag{11}$$

But from the Einstein model

$$\frac{R_g}{c_{p_1}} = \frac{c_{p_1} - c_{v_1}}{c_{p_1}} = \frac{R_g\left[\frac{7}{2} + \left(\frac{T_r}{T}\right)^2 \frac{e^{\frac{T_r}{T}}}{\{e^{\frac{T_r}{T}} - 1\}^2}\right] - \left[\frac{5}{2} + \frac{e^{\frac{T_r}{T}}(\frac{T_r}{T})^2}{\{e^{\frac{T_r}{T}} - 1\}^2}\right] R_g}{R_g\left[\frac{7}{2} + \left(\frac{T_r}{T}\right)^2 \frac{e^{\frac{T_r}{T}}}{\{e^{\frac{T_r}{T}} - 1\}^2}\right]}$$
$$= \frac{\frac{2}{7}}{\left[1 + \frac{2}{7}\left(\frac{T_r}{T}\right)^2 \frac{e^{\frac{T_r}{T}}}{\{e^{\frac{T_r}{T}} - 1\}^2}\right]} \tag{12}$$

At moderate temperatures (<450 K) where the specific heats of the gas can be treated as constants

$$\{e^{\frac{T_r}{T}} - 1\}^2 \approx \{e^{\frac{3070}{450}} - 1\}^2 \approx 8.40 \times 10^5$$
$$\gg \frac{2}{7}\left(\frac{T_r}{T}\right)^2 e^{\frac{T_r}{T}} \approx \frac{2}{7}\left(\frac{3070}{450}\right)^2 e^{\frac{3070}{450}} \approx 1.22 \times 10^4 \tag{13}$$

and Eq. (12) reduces to

$$\frac{R_g}{c_{p1}} = \left(\frac{\gamma_1 - 1}{\gamma_1}\right) = \frac{2}{7} \tag{14}$$

Equation (14) holds for *any diatomic gas* at temperatures where the specific heats are constant. In Eq. (1) γ_1 represents the "normal" room temperature value for the gas-specific heat ratio. Substituting Eq. (14) into Eq. (11), results in a more general expression

$$T_2 + \frac{V_2^2}{2c_{p1}} + \left(\frac{\gamma_1 - 1}{\gamma_1}\right)\frac{T_r}{\{e^{\frac{T_r}{T_2}} - 1\}}$$
$$= T_1 + \frac{V_1^2}{2c_{p1}} + \left(\frac{\gamma_1 - 1}{\gamma_1}\right)\frac{T_r}{\{e^{\frac{T_r}{T_1}} - 1\}} \tag{15}$$

Using the definition for the stagnation temperature of an ideal gas

$$T_0 = T + \frac{V^2}{2c_p} \tag{16}$$

and substituting Eq. (16) into Eq. (15), the result is

$$T_{0_2} = T_{0_1} + \left(\frac{\gamma_1 - 1}{\gamma_1}\right) T_r\left[\frac{e^{\frac{T_r}{T_2}} - e^{\frac{T_r}{T_1}}}{\{e^{\frac{T_r}{T_2}} - 1\}\{e^{\frac{T_r}{T_1}} - 1\}}\right] \tag{17}$$

The last term on the right-hand side of Eq. (17) is the vibrational correction for the flow across the shock wave. Because $T_2 > T_1$ across the shock wave, the correction term has a negative magnitude and Eq. (17) shows the well-known result that stagnation temperature drops across a nonideal shock wave. Equations (16) and (17) are valid for both normal and oblique shock wave where the gas species concentrations do not change across the shock wave.

C. Oblique Shock Wave Geometry

The geometry of the oblique shock wave [10] will now be applied to develop an algorithm that is specifically valid for shock discontinuities that are oblique to the freestream flow velocity vector. Figure 1 shows the steady-state flow geometry across an oblique shock wave. Following a well-known analysis procedure, the flow upstream of the shock wave is partitioned into flow components normal and tangential to the shock wave. The shock wave angle is β, and the flow-turning angle downstream of the shock wave is θ. The steady-state conservation equations are as follows:

1) ContinuityL

$$\rho_1 u_1 = \rho_2 u_2 \tag{18a}$$

2) Momentum:

$$w_1 = w_2 \tag{18b}$$

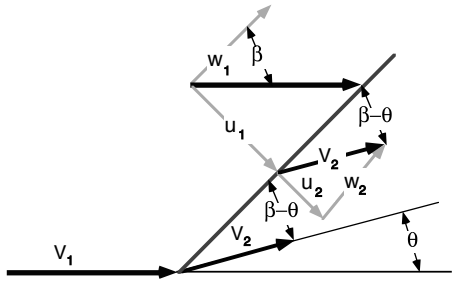

Fig. 1 Flow geometry across oblique shock wave.

$$p_1 + \rho_1 u_1^2 = p_2 + \rho_2 u_2^2 \tag{18c}$$

Using the ideal-gas law to write temperature in terms of pressure and density, and substituting in the continuity and momentum equations,

$$\frac{T_2}{T_1} = \frac{p_2}{p_1}\frac{\rho_1}{\rho_2} = \frac{p_2}{p_1}\frac{u_2}{u_1} = \frac{\left[1 + \frac{\rho_1}{p_1}u_1^2\right]u_2}{\left[1 + \frac{\rho_2}{p_2}u_2^2\right]u_1} = \frac{\left[1 + \frac{u_1^2}{R_g T_1}\right]u_2}{\left[1 + \frac{u_2^2}{R_g T_2}\right]u_1} \tag{19}$$

Solving for T_2 in terms of T_1,

$$T_2 + \frac{u_2^2}{R_g} = \left[T_1 + \frac{u_1^2}{R_g}\right]\frac{u_2}{u_1} \tag{20}$$

Also because Eq. (17) can be written as

$$T_2 + \frac{u_2^2 + w_2^2}{2c_{p1}} + \left(\frac{\gamma_1 - 1}{\gamma_1}\right)\frac{T_r}{\{e^{\frac{T_r}{T_2}} - 1\}} = T_1 + \frac{u_1^2 + w_1^2}{2c_{p1}} + \left(\frac{\gamma_1 - 1}{\gamma_1}\right)\frac{T_r}{\{e^{\frac{T_r}{T_1}} - 1\}} \tag{21}$$

the flow-turning angle can be written in terms of the shock wave angle using geometric arguments,

$$\frac{u_2}{u_1} = \frac{\tan(\beta - \theta)}{\tan(\beta)} \tag{22}$$

Expanding $\tan(\beta - \theta)$ collecting terms, Eq. (22) can be reduced to

$$\tan(\theta) = \frac{[1 - (u_2/u_1)]}{(u_2/u_1)\tan(\beta)} \tag{23}$$

Because $w_1 = w_2$, Eq. (17) can be written in terms of the normal velocity component only, and the collected conservation equations for the real-gas (vibrational-mode excited) oblique shock wave are

$$T_2 + \frac{u_2^2}{R_g} = \left[T_1 + \frac{[V_1 \sin(\beta)]^2}{R_g}\right]\frac{u_2}{V_1 \sin(\beta)} \tag{24a}$$

$$T_2 + \frac{u_2^2}{2c_{p1}} + \left(\frac{\gamma_1 - 1}{\gamma_1}\right)\frac{T_r}{\{e^{\frac{T_r}{T_2}} - 1\}} = T_1 + \frac{[V_1 \sin(\beta)]^2}{2c_{p1}} + \left(\frac{\gamma_1 - 1}{\gamma_1}\right)\frac{T_r}{\{e^{\frac{T_r}{T_1}} - 1\}} \tag{24b}$$

$$\tan(\theta) = \frac{[V_1 \sin(\beta) - u_2]}{[V_1 \cos(\beta) + u_2 \tan(\beta)]} \tag{24c}$$

Equations (24a–24c) are a nonlinear set of three equations with the parameters T_2, u_2, β as dependent variables, and the $\{\theta, V_1, T_1\}$ as independent variables. Unlike the ideal-gas oblique shock wave equations, which have only M_1 and θ as independent variables, these equations have an extra degree of freedom. This degree of freedom is a consequence of the vibrational-mode excitation, and the gas-specific heats being influenced by the temperature change across the shock wave.

D. Solution Procedure for Two-Dimensional Flowfields

Because the flow-turning angle is written explicitly in terms of the shock wave angle and the incoming flow velocity, it is convenient to partition the numerical solution into two parts, 1) an inner loop iteration and 2) an outer loop iteration. In this approach a guess is made for the shock wave angle, based on the ideal oblique shock wave equations, Eqs. (24a) and (24b) are solved using a 2×2 Newton–Raphson [11] root solver to calculate $\{u_2, T_2\}$, and the flow-turning angle is calculated using Eq. (24c). The freestream shock wave angle is reevaluated using a separate Newton solver, and the solution is iterated until convergence upon the actual flow-turning angle. Once the state vector $\{T_2, u_2, \beta\}$ has been solved, then other downstream parameters of interest can be directly calculated. Partitioning the algorithm into separate solutions for $\{u_2, T_2\}$ and β saves a considerable number of execution steps when compared to solving a 3×3 system directly.

1. *Solving for T_2, u_2*

Starting with an initial estimate for the shock angle $\beta^{(j)}$ (calculated using the ideal-gas equations), define the functions

$$\begin{aligned} &T_2 + \frac{u_2^2}{2c_{p1}} + \left(\frac{\gamma_1 - 1}{\gamma_1}\right)\frac{T_r}{\{e^{\frac{T_r}{T_2}} - 1\}} \\ &\quad - \left\{T_1 + \frac{[V_1 \sin(\beta^{(j)})]^2}{2c_{p1}} + \left(\frac{\gamma_1 - 1}{\gamma_1}\right)\frac{T_r}{\{e^{\frac{T_r}{T_1}} - 1\}}\right\} \\ &\quad = f(T_2, u_2) = 0 \\ &T_2 + \frac{u_2^2}{R_g} - \left[T_1 + \frac{[V_1 \sin(\beta^{(j)})]_1^2}{R_g}\right]\frac{u_2}{[V_1 \sin(\beta^{(j)})]} \\ &\quad = g(T_2, u_2) = 0 \end{aligned} \tag{25}$$

The iterative algorithm for $\{T_2, u_2\}$ is

$$\begin{aligned} T_2^{(n+1)} &= T_2^{(n)} - \frac{f(T_2^{(n)}, u_2^{(n)})\left[\frac{\partial g(T_2,u_2)}{\partial u_2}\right]_{|n} - \left[\frac{\partial f(T_2,u_2)}{\partial u_2}\right]_{|n} g(T_2^{(n)}, u_2^{(n)})}{\left[\frac{\partial f(T_2^{(n)},u_2^{(n)})}{\partial T_2}\right]_{|n}\left[\frac{\partial g(T_2,u_2)}{\partial u_2}\right]_{|n} - \left[\frac{\partial f(T_2,u_2)}{\partial u_2}\right]_{|n}\left[\frac{\partial g(T_2,u_2)}{\partial T_2}\right]_{|n}} \\ u_2^{(n+1)} &= u_2^{(n)} - \frac{\left[\frac{\partial f(T_2^{(n)},u_2^{(n)})}{\partial T_2}\right]_{|n} g(T_2^{(n)}, u_2^{(n)}) - f(T_2^{(n)}, u_2^{(n)})\left[\frac{\partial g(T_2,u_2)}{\partial T_2}\right]_{|n}}{\left[\frac{\partial f(T_2^{(n)},u_2^{(n)})}{\partial T_2}\right]_{|n}\left[\frac{\partial g(T_2,u_2)}{\partial V_2}\right]_{|n} - \left[\frac{\partial f(T_2,u_2)}{\partial V_2}\right]_{|n}\left[\frac{\partial g(T_2,u_2)}{\partial T_2}\right]_{|n}} \end{aligned} \tag{26}$$

In Eq. (26), the parameters V_1, T_1, and $\beta^{(j)}$ are inputs to the solver, n is the current inner loop iteration index, and $\{T_2^{(n)}, u_2^{(n)}\}$ are the current iteration values for the state vector. The elements of the Jacobean matrix are Eq. (26)

$$\begin{bmatrix} \frac{\partial f(T_2,u_2)}{\partial T_2} = \left(\frac{\gamma_1 - 1}{\gamma_1}\right)\frac{e^{\frac{T_r}{T_2}}\left[\frac{T_r}{T_2}\right]^2}{\{e^{\frac{T_r}{T_2}} - 1\}} + 1 & \frac{\partial f(T_2,u_2)}{\partial u_2} = \frac{u_2}{c_{p1}} \\ \frac{\partial g(T_2,u_2)}{\partial T_2} = 1 & \frac{\partial g(T_2,u_2)}{\partial u_2} = \frac{2u_2}{R_g} - \frac{T_1 + \frac{[V_1 \sin(\beta^{(j)})]^2}{R_g}}{[V_1 \sin(\beta^{(j)})]} \end{bmatrix} \tag{27}$$

The inner loop stage of the algorithm iteration reaches convergence when

$$\sqrt{\left(\frac{u_2^{(n+1)} - u_2^{(n)}}{u_2^{(n)}}\right)^2 + \left(\frac{T_2^{(n+1)} - T_2^{(n)}}{T_2^{(n)}}\right)^2} < \varepsilon \tag{28}$$

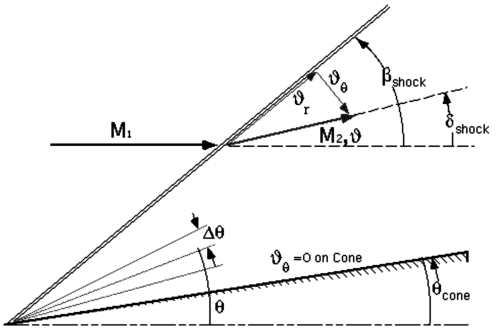

Fig. 2 Conical shock wave geometry.

2. Solving for β

Using a converged value for u_2, a new value for β is calculated using the iteration equation,

$$\beta^{(j+1)} = \beta^{(j)} - \frac{\partial \beta^{(j)}}{\partial \theta}[\theta^{(j)} - \theta] \tag{29a}$$

In Eq. (29a)

$$\theta^{(j)} = \tan^{-1}\left[\frac{[V_1 \sin(\beta^{(j)}) - u_2^{(j)}]}{\left[V_1 \cos(\beta^{(j)}) + u_{22}^{(j)} \tan(\beta^{(j)})\right]}\right] \tag{29b}$$

and

$$\frac{\partial \beta^{(j)}}{\partial \theta} = \frac{1}{1 - \frac{1}{2}\sin[2(\beta^{(j)} - \theta)]\tan(\beta^{(j)})} \tag{29c}$$

Equations (25–29) are iterated to convergence. The outer loop of the algorithm reaches convergence when

$$\left\| \frac{[\theta^{(j+1)} - \theta]}{[\theta]} \right\| < \delta \tag{30}$$

Once the parameters $\{T_2, u_2, \beta\}$ have been calculated, the remainder of the properties downstream of the shock wave can be computed. Referring to Fig. 2, the velocity and Mach and pressure ratio across number the shock wave are calculated by

$$V_2 = \frac{u_2}{\sin(\beta - \theta)} \tag{31a}$$

$$M_2 = \frac{V_2}{\sqrt{\gamma_2 R_g T_2}} \tag{31b}$$

$$\frac{p_2}{p_1} = \frac{[1 + \gamma_1 (M_1 \sin\beta)^2]}{[1 + \gamma_2 (M_2 \sin(\beta - \theta))^2]} \tag{31c}$$

In Eq. (31b), the ratio of specific heats is calculated using Eqs. (3) and (4).

E. Solution Procedure for Conical Flowfields

The procedure presented in the previous section can be modified for conical flowfields by assuming an initial shock angle, and using the algorithm of Eqs. (25–28), Eq. (31) can compute the properties immediately behind the conical shock wave. Figure 2 shows the conical shock wave geometry.

Just behind the conical shock wave

$$\vartheta = \sqrt{\frac{[(\gamma - 1)/2]M_2^2}{\{1 + [(\gamma - 1)/2]M_2^2\}}} \tag{32a}$$

and the radial and circumferential velocity components are

$$\vartheta_r = \vartheta \cos(\beta_{\text{shock}} - \delta_{\text{shock}}) \tag{32b}$$

$$\vartheta_\theta = -\vartheta \sin(\beta_{\text{shock}} - \delta_{\text{shock}}) \tag{32c}$$

Using Eqs. (32a) and (32b) as starting conditions, the Taylor–Maccoll equations [12]

$$\begin{bmatrix} \frac{\partial \vartheta_r}{\partial \theta} \\ \frac{d\vartheta_\theta}{d\theta} \end{bmatrix} = \begin{bmatrix} \vartheta_\theta \\ \frac{\vartheta_\theta^2 \vartheta_r - \frac{\gamma_2 - 1}{2}(1 - \vartheta_r^2 - \vartheta_\theta^2)(2\vartheta_r + \vartheta_\theta \cot(\theta))}{[\frac{\gamma_2 - 1}{2}(1 - \vartheta_r^2 - \vartheta_\theta^2) - \vartheta_\theta^2]} \end{bmatrix} \tag{33}$$

are numerically integrated for decrements of θ until $\vartheta_\theta = 0$. The value of θ corresponding to $\vartheta_\theta = 0$ represents the solid cone boundary corresponding the input flow conditions and the assumed shock angle. On the surface of the cone $\vartheta = \vartheta_r$, and

$$M_{\text{cone}} = \sqrt{\frac{2}{(\gamma_2 - 1)}\left[\frac{(\vartheta_{\text{cone}})^2}{1 - (\vartheta_{\text{cone}})^2}\right]} \tag{34}$$

Assuming the flow behind the conical shock wave is isentropic and that variations in γ_2 are negligible behind the shock wave, the temperature and pressure ratios are given by

$$\frac{p_{\text{cone}}}{p_1} = \left[\frac{1 + \frac{(\gamma_2 - 1)}{2}(M_2)^2}{1 + \frac{(\gamma_2 - 1)}{2}(M_{\text{cone}})^2}\right]^{\frac{\gamma_2}{\gamma_2 - 1}} \frac{p_2}{p_1} \tag{35a}$$

and

$$\frac{T_{\text{cone}}}{T_1} = \left[\frac{1 + \frac{(\gamma_2 - 1)}{2}(M_2)^2}{1 + \frac{(\gamma_2 - 1)}{2}(M_{\text{cone}})^2}\right] \frac{T_2}{T_1} \tag{35b}$$

For Eqs. (35a) and (35b), T_2 and p_2 are the temperature and pressure behind the shock wave as computed using the algorithmsin Eqs. (25–31).

III. Results and Discussion

These sections assess results from calculations using the vibrational-mode real-gas model derived in the previous section. Because of the extra degree of freedom (temperature dependence of gas properties) one cannot produce a general $\beta - \theta$-Mach diagram ([10]) as has traditionally been done for the ideal-gas oblique shock wave. Instead an illustrative comparison of the derived model and the ideal gas will be presented for a 15 deg two-dimensional wedge angle at increasing Mach numbers. A similar comparison will be presented for a 15 deg conical flowfield. Finally, the two-dimensional model

Table 1 Comparison of vibrational-mode oblique shock wave model to ideal-gas model for two-dimensional 15 deg wedge flowfield

Vibrational-mode oblique shock wave model						Ideal-gas oblique shock wave model				
M_1	β, deg	M_2	T_2/T_1	To_2/To_1	p_2/p_1	β, deg	M_2	T_2/T_1	To_2/To_1	p_2/p_1
4.0	27.056	2.9307	1.5454	0.9968	3.6988	27.0711	2.9271	1.5483	1.0000	3.7004
8.0	20.7759	4.8136	2.4702	0.9695	9.2743	20.8691	4.7425	2.5107	1.0000	9.3117
12.0	19.2225	5.8959	3.8579	0.9091	18.239	19.4234	5.6469	4.0406	1.0000	18.4181
16.0	18.5269	6.6041	5.6132	0.8581	30.5535	18.8760	6.1121	6.1637	1.0000	31.1043
24.0	17.8974	7.4285	10.2179	0.8095	65.2719	18.4687	6.5258	12.2129	1.0000	67.2941

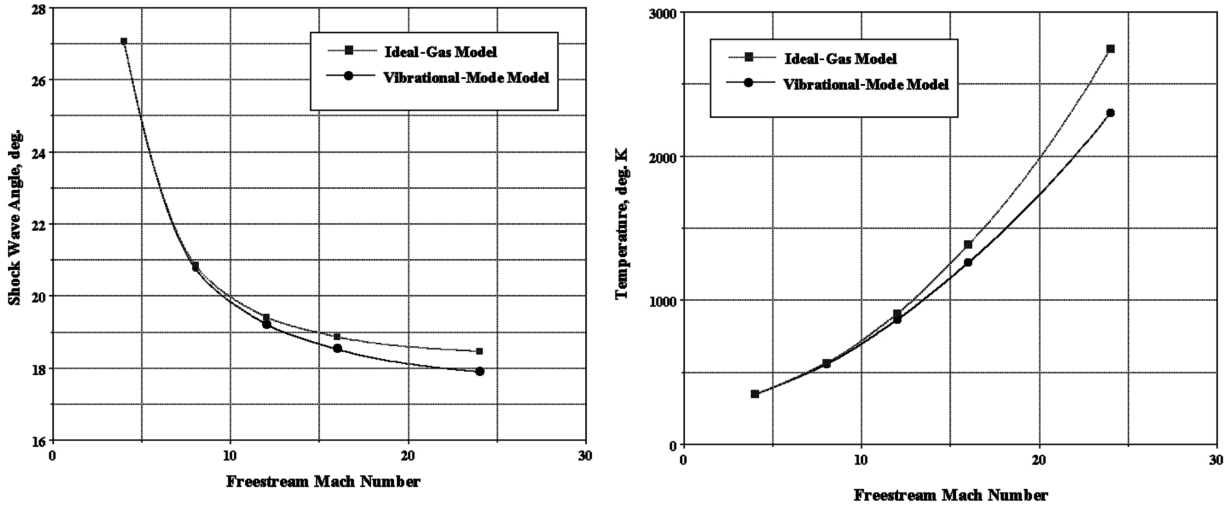

a) Shock wave angle **b) Temperature behind shock wave**

Fig. 3 Comparison of properties for ideal-gas and vibrational oblique shock wave models.

calculations for a 15 deg wedge will be compared against equilibrium gas–chemistry calculations to demonstrate the comparative accuracies and regimes of applicability.

A. Einstein Thermodynamic Model

Table 1 compares the calculations for the vibrational-mode real-gas model to ideal-gas solutions for a 15 deg wedge angle for five different freestream Mach numbers, 4.0, 8.0, 12.0, 16.0, and 24.0. In each case the freestream ambient temperature is assumed to be 225 K and corresponds to a typical midlevel stratospheric temperature. The working fluid is assumed to be standard dry air. Figure 3 compares the shock wave angle and temperature behind the shock wave for the *vibrational-mode* and *ideal-gas* oblique shock wave models.

Two well-known results are represented in Fig. 3 as follows: 1) real-gas effects cause the shock wave to lie closer to the body than is represented by the ideal-gas calculations, and 2) there is a significantly lower temperature behind the shock wave than predicted by ideal-gas calculations. These phenomena are a consequence of the energy that is absorbed to excite the vibrational modes of the air molecule species.

B. Nonideal Shock Wave Enthalpy Balance

The calculations presented in the previous subsection were repeated for supersonic flow over a 15 deg cone at zero-incidence angle. Results are presented in Table 2. As with the earlier comparisons the freestream ambient temperature is assumed to be 225 K, even though the conical shock wave angle is only slightly influenced by the excitation of the vibrational modes of the gas. The reduction in γ behind the conical shock wave has a significant effect on the resulting temperature and pressure distribution. There is a reduction in the strength of the compression and the pressures and temperatures on the surface of the cone are significantly lower than occurs in the ideal-gas scenario. This *three-dimensional relief* is a well-known phenomenon. Figure 4 compares the shock wave angle and temperature behind the shock wave for the vibrational-mode and ideal-gas conical shock wave models.

C. Comparison to Equilibrium Gas–Chemistry Calculations

In this section the real-gas oblique shock wave model presented in the previous sections is compared to calculations performed using the equilibrium gas–chemistry code chemical equilibrium with applications (CEA) [13,14]. The CEA code was developed at NASA Glenn Research Center and has been successfully applied for the analysis of rocket combustion, detonation, and flow across nonadiabatic shock waves. The code posits chemical reactions across the shock wave and then minimizes the Gibbs free energy [15] to reach thermodynamic and transport properties at chemical equilibrium. The code has extensive internal libraries for gas thermodynamic and transport properties including air at standard and nonstandard conditions.

CEA was applied to this problem by assuming a starting shock wave angle based on ideal-gas calculations. It is assumed that for the flow behind the shock wave a sufficient distance has been allowed for the gas to reach chemical equilibrium. The component of Mach number normal to the shock wave was calculated and fed into CEA as the input Mach number along with the ambient temperature and pressure levels. The code calculates the properties on the downstream side of the shock wave. Using these properties and Eqs. (23) and (29), a new value for the shock wave angle is calculated outside of the CEA program, a new normal component of freestream Mach number is computed, and the tedious process is repeated until convergence is reached.

Figures 5a–5d show the results of the calculations for a 15 deg wedge angle for input Mach numbers from 2.0 to 30.0, assuming an input temperature of 225°F. Figure 5a plots the temperature ratio versus freestream Mach number, Fig. 5b plots the pressure ratio, Fig. 5c plots the downstream Mach number, and Fig. 5d plots the ratio of specific heats downstream of the shock wave. The ideal-gas and vibrational model calculations are presented for comparison purposes. For this 15 deg wedge calculation the comparisons

Table 2 Comparison of vibrational-mode oblique shock wave model to ideal-gas model for 15 deg conical flowfield at zero incidence angle

Vibrational-mode oblique shock wave model						Ideal-gas oblique shock wave model				
M_1	β, deg	M_2	T_2/T_1	To_2/To_1	p_2/p_1	β, deg	M_2	T_2/T_1	To_2/To_1	p_2/p_1
4.0000	21.7900	3.2166	1.3682	0.9988	2.794	21.7900	3.2156	1.3693	1.0000	2.8014
8.0000	17.9288	5.3057	2.0894	0.9835	7.0224	17.9340	5.1942	2.1581	1.0000	7.5506
12.0000	17.1000	6.7313	3.0310	0.9325	10.9084	17.1275	6.1964	3.4344	1.0000	15.4202
16.0000	16.7876	8.0832	3.8409	0.8817	13.9848	16.8265	6.7169	5.2090	1.0000	26.4022
24.0000	16.5693	9.2778	6.7925	0.8176	18.9630	16.6025	7.1833	10.2676	1.0000	57.7366

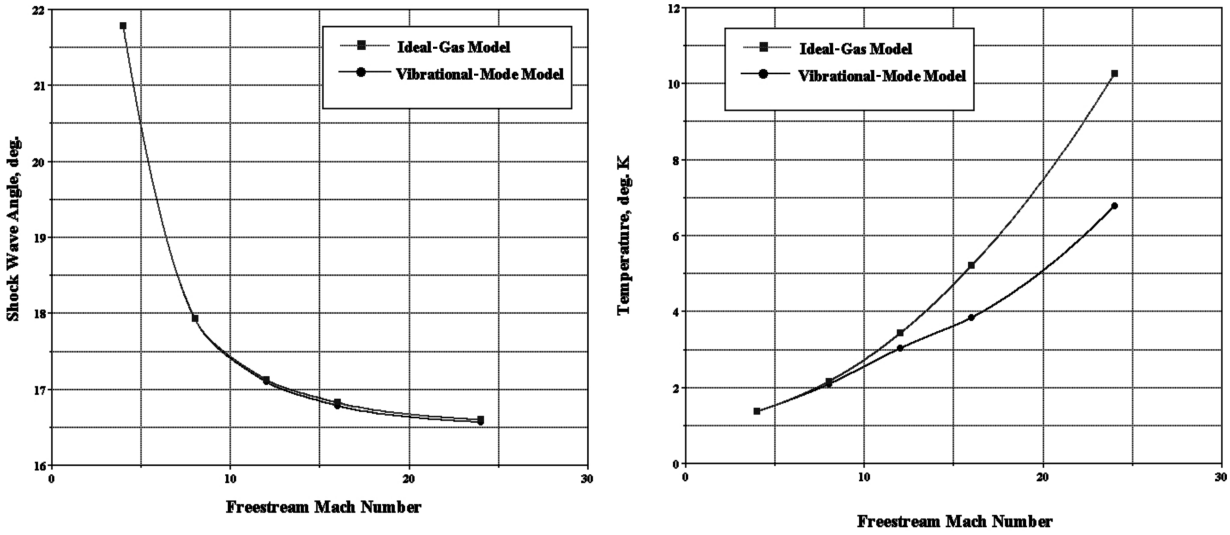

a) Shock wave angle **b) Temperature behind shock wave**

Fig. 4 Comparison of properties for ideal-gas and vibrational conical shock wave models.

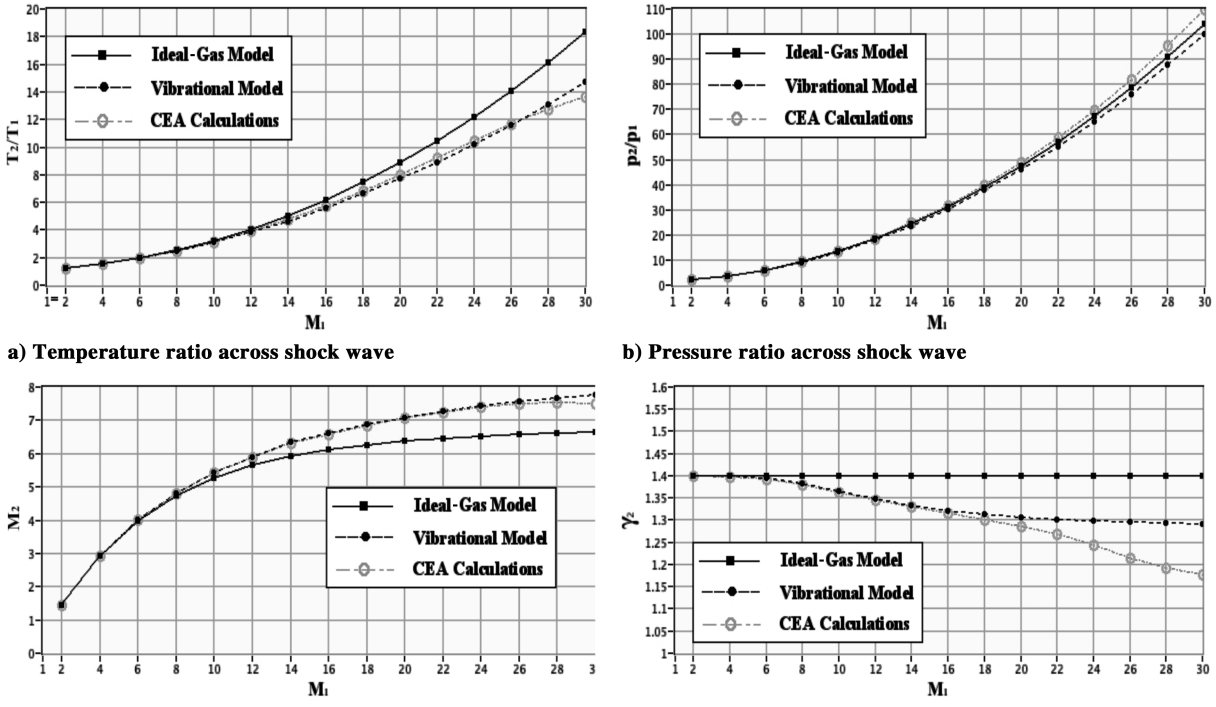

a) Temperature ratio across shock wave **b) Pressure ratio across shock wave**

c) Mach number behind shock wave **d) Specific heat ratio behind shock wave**

Fig. 5 Comparison of ideal-gas and vibrational oblique shock wave models to CEA calculations.

between the *vibrational-gas* model and the CEA model are excellent up to approximately Mach 20. When the Mach number exceeds 20, the curves begin to diverge. This divergence is especially large for γ_2. At this Mach number the gas dissociation becomes significant and the *single species concentration approximation* is no longer accurate.

This premise is supported by the data presented in Table 3. Table 3 shows the gas species concentration downstream of the oblique shock wave by mole factions as calculated by CEA for freestream Mach numbers varying from 4 to 30. Although some minor nitrogen dissociation behind the shock wave begins to occur at Mach numbers as low 8.0, the concentrations of N_2 and O_2 behind the shock wave begin to drop rapidly for between freestream Mach numbers of 16 and 20. Beyond Mach 20, the concentrations of atomic oxygen and NO rise rapidly. At Mach 30 the ratio of atomic-to-molecular oxygen is approximately 29% and the ratio of NO-to-molecular nitrogen is approximately 6%. Thus the gaseous mixture here is significantly different from air at lower temperatures.

Further support for this premise is offered by Fig. 6 where the *molecular weight* and *gas constant* behind the shock wave are plotted as a function of the freestream Mach number. The values remain essentially constant until the freestream Mach number reaches 20.0, and then rapidly depart from the initial value. Because molecular weight and the gas constant are constant for a given gas species concentration, these rapidly changing properties mean that the gas species concentration is changing rapidly.

The large number of manual iterations required for performing the CEA calculations on a 15 deg conical flowfield made this calculation

Table 3 Equilibrium gas species concentration by mole fraction behind 15 deg wedge shock wave

Gas species	Mach 4	Mach 8	Mach 12	Mach 16	Mach 20	Mach 24	Mach 28	Mach 30
O3	0.00E + 00	0.00E + 00	0.00E + 00	0.00E + 00	0.00E + 00	2.12E − 08	8.72E − 08	1.32E − 07
N2O	0.00E + 00	0.00E + 00	0.00E + 00	1.79E − 08	2.02E − 07	9.57E − 07	2.38E − 06	3.16E − 06
N	0.00E + 00	0.00E + 00	0.00E + 00	0.00E + 00	0.00E + 00	6.10E − 08	4.05E − 06	1.55E − 05
NO2	0.00E + 00	2.76E − 08	5.20E − 07	2.96E − 06	8.85E − 06	1.78E − 05	2.56E − 05	2.75E − 05
CO	0.00E + 00	0.00E + 00	0.00E + 00	0.00E + 00	1.71E − 07	1.10E − 05	8.89E − 05	1.44E − 04
CO2	3.19E − 04	3.19E − 04	3.19E − 04	3.19E − 04	3.19E − 04	3.08E − 04	2.26E − 04	1.68E − 04
Ar	9.37E − 03	9.37E − 03	9.37E − 03	9.37E − 03	9.37E − 03	9.35E − 03	9.25E − 03	9.15E − 03
NO	0.00E + 00	5.72E − 09	7.19E − 06	3.93E − 04	4.13E − 03	1.70E − 02	3.61E − 02	4.44E − 02
O	0.00E + 00	0.00E + 00	0.00E + 00	1.17E − 07	6.57E − 05	2.98E − 03	2.45E − 02	4.61E − 02
O2	2.10E − 01	2.10E − 01	2.09E − 01	2.09E − 01	2.07E − 01	1.99E − 01	1.77E − 01	1.59E − 01
N2	7.81E − 01	7.81E − 01	7.81E − 01	7.81E − 01	7.79E − 01	7.71E − 01	7.53E − 01	7.41E − 01

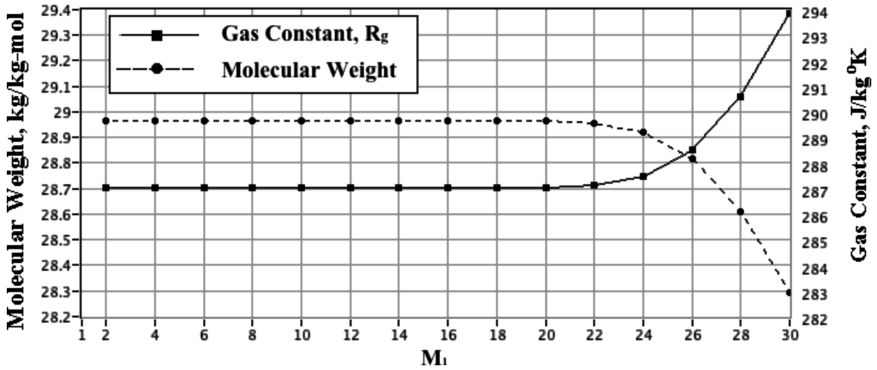

Fig. 6 Molecular weight and gas constant for flow conditions behind 15 deg wedge shock wave.

infeasible. However, because of the three-dimensional relief effect, it can be reasoned that the vibrational model will agree with the CEA calculations for Mach numbers slightly higher than the Mach 20 threshold shown in Figs. 5 and 6. In any case for hypersonic shapes of practical interest, it appears that Mach 20 is near the upper limit of applicability of the vibrational-mode oblique shock wave model developed in the previous sections.

IV. Summary and Concluding Remarks

For conceptual design, engineering codes are still the preferred method for aerospace vehicles. Their use in the early stages of design enables higher fidelity CFD calculations and/or wind-tunnel tests to be performed on more mature vehicle concepts and can shave many months off of the design process. A widely used engineering code for conceptual level supersonic/hypersonic aerodynamic prediction is the S/HABP. For bodies with relatively sharp leading edges, S/HABP uses the tangent-wedge, or tangent-cone methods to calculate the pressures and inviscid flow temperatures on arbitrarily shaped bodies and lifting surfaces. The wedge and cone methods are commonly used in hypersonic analysis methods because they are relatively simple but yield surprisingly accurate results. Unfortunately, the tangent-wedge and tangent-cone analysis tools have always missed a key element necessary for accurate hypersonic flowfield design, and that is the ability to systematically account for the effects of real-gas flow across the oblique shock wave. This paper derives an extension to the classical oblique shock wave equations where the effects of real-gas flow changes across the shock wave are modeled using theoretical models borrowed from statistical mechanics. The oblique shock wave model extensions are directly applicable for use in tangent-wedge engineering models and are easily adapted for conical flowfields.

For flight conditions where gas dissociation does not occur, that is for a single species gas concentration, the specific heats are strongly a function of temperature and weakly a function of pressure. This physical situation frequently occurs behind hypersonic oblique, conical, or detached shock waves away from the stagnation point. Here the shock wave is angled relative to the incoming flow and the subsequent compression and temperature rise is sufficient to excite vibrational modes of the gas molecules, but insufficient to cause gas dissociation. For engineering purposes, the Einstein model for a diatomic gas can be used to approximate the flow conditions. Using an enthalpy balance across the shock wave, the Einstein model is analytically integrated to give a relationship of temperature and velocity on the downstream side of the shock wave in term of the upstream flow properties. This relationship replaces the energy equation used to develop the oblique shock wave equations for the traditional ideal-gas analysis. The methods are modified for conical (tangent-cone) flowfields by assuming an initial shock angle, and using the modified oblique shock algorithm to compute the properties immediately behind the conical shock wave. The resulting model is compared to equilibrium real-gas calculations for a 15 deg wedge and is shown to give very accurate results well up into the hypersonic flow regime, approximately Mach 20. A detailed solution algorithm is presented and represents an important extension to the tangent-wedge and tangent-cone analysis tools.

References

[1] Blake, W., "Missile DATCOM Users Manual," AFRLVA WP-TR-1998-3009, Feb. 1998.

[2] Gentry, A. E., Smyth, D. N., and Oliver, W. R., "The Mark IV Supersonic-Hypersonic Arbitrary-Body Program," McDonnell-Douglas Corporation, TR AFFDL-TR-73-159, Nov. 1973.

[3] Anderson, J. D., *Hypersonic and High Temperature Gas Dynamics*, McGraw–Hill Inc., New York, 1989, Chap. 3.

[4] Corda, S., and Anderson, J. D., Jr., "Viscous Optimized Waveriders Designed from Axisymmetric Flow Fields," AIAA Paper 88-0369, 1988.

[5] Lees, L., "Hypersonic Flow," *Journal of Spacecraft and Rockets*, Vol. 40, No. 5, Sept.–Oct. 2003, pp. 700–735.

[6] Mills, A. F., *Heat Transfer*, Irwin Publishing, Homewood, IL, 1992, Chap. 4.

[7] Navarro, L., "Gibbs, Einstein and the Foundations of Statistical Mechanics," *Archives for History of Exact Science*, Vol. 53, No. 2, 1998, pp. 147–180.

[8] Anderson, J. D., *Hypersonic and High Temperature Gas Dynamics*, AIAA, Reston, VA, 2000, pp. 438–443. (Originally published by McGraw–Hill, 1989).

[9] Shapiro, A. H., *Compressible Fluid Flow*, Vol. 1, Wiley, New York, 1953, pp. 96–97.

[10] Anderson, J. D., Jr., *Modern Compressible Flow with Historical Perspective*, 3rd ed., McGraw–Hill Higher Education, New York, 2003, Chap. 4.

[11] Rade, L., and Westergren, B., *Beta β Mathematics Handbook*, 2nd ed., CRC Press, Boca Raton, FL, 1990, pp. 331–332.

[12] Anderson, J. D., Jr., *Modern Compressible Flow with Historical Perspective*, 3rd ed., McGraw–Hill Higher Education, New York, 2003, Chap. 10.

[13] Gordon, S., and McBride, B. J., "Computer Program for Calculation of Complex Chemical Equilibrium Compositions and Applications," NASA RP-1311, 1994.

[14] Gordon, S., and McBride, B. J., "Computer Program for Calculation of Complex Chemical Equilibrium Compositions and Applications, Vol. 2, Users Manual and Program Descriptions," NASA RP-1311, 1994.

[15] Zeleznik, F. J., and Gordon, S., "Calculation of Complex Chemical Equilibria," *Journal of Industrial and Engineering Chemistry*, Vol. 60, No. 6, 1968, pp. 27–57.

C. Kaplan
Associate Editor